


FULL PAPER

Open Access



# Exploring planets and asteroids with 6DoF sensors: Utopia and realism

Felix Bernauer<sup>1\*</sup> , Raphael F. Garcia<sup>2</sup>, Naomi Murdoch<sup>2</sup>, Veronique Dehant<sup>3</sup>, David Sollberger<sup>4</sup>, Cedric Schmelzbach<sup>4</sup>, Simon Stähler<sup>4</sup>, Joachim Wassermann<sup>1</sup>, Heiner Igel<sup>1</sup>, Alexandre Cadu<sup>2</sup>, David Mimoun<sup>2</sup>, Birgit Ritter<sup>3</sup>, Valerio Filice<sup>3</sup>, Özgür Karatekin<sup>3</sup>, Luigi Ferraioli<sup>4</sup>, Johan O. A. Robertsson<sup>4</sup>, Domenico Giardini<sup>4</sup>, Guillaume Lecamp<sup>5</sup>, Frederic Guattari<sup>5</sup>, Jean-Jacques Bonnefois<sup>5</sup> and Sebastien de Raucourt<sup>6</sup>

## Abstract

A 6 degrees-of-freedom (6DoF) sensor, measuring three components of translational acceleration and three components of rotation rate, provides the full history of motion it is exposed to. In Earth sciences 6DoF sensors have shown great potential in exploring the interior of our planet and its seismic sources. In space sciences, apart from navigation, 6DoF sensors are, up to now, only rarely used to answer scientific questions. As a first step of establishing 6DoF motion sensing deeper into space sciences, this article describes novel scientific approaches based on 6DoF motion sensing with substantial potential for constraining the interior structure of planetary objects and asteroids. Therefore we estimate 6DoF-signal levels that originate from lander–surface interactions during landing and touchdown, from a body's rotational dynamics as well as from seismic ground motions. We discuss these signals for an exemplary set of target bodies including Dimorphos, Phobos, Europa, the Earth's Moon and Mars and compare those to self-noise levels of state-of-the-art sensors.

**Keywords:** Planetary exploration, Planetary seismology, Librations, Tides, 6DoF sensors

## Introduction

How did our solar system evolve? Are there habitable worlds among recently discovered extra-solar planets? Where, and in which form, does life exist outside our Earth? These are key questions that planetary scientists try to answer. Investigating the internal structure of planetary objects and asteroids can provide important information to these key questions. The observation of elastic wave propagation on the surface of planetary bodies allows the recovery of information on structural properties down to the body's deep interior, depending on the characteristics of the seismic source including quakes, atmospheric processes, tides and impacts. However, classical methods for planetary exploration like seismology

or gravimetry often suffer from large uncertainties that simply originate from the low number of instruments utilized on planetary objects compared to our planet Earth.

For example, during the Apollo lunar missions five seismometers were deployed on the near side of the Moon between 1969 and 1972 (Latham et al. 1969, 1971), four of them operating continuously until 1977. Despite the sparsity of this lunar seismic network, important conclusions on the internal structure and seismic sources could be drawn (see Garcia et al. (2019) for a recent review). The majority of recorded events appear to be small local moonquakes triggered by diurnal temperature changes, so-called thermal moonquakes (Duennebieer and Sutton 1974). Periodic seismic activity connected with tides (Minshull and Gouly 1988; Lammlein et al. 1974; Lammlein 1977; Nakamura 2005) could be located in the Moon's deep interior (Nakamura et al. 1982; Nakamura 2003). Wavefields with extremely strong scattering and low attenuation near the surface were observed for

\*Correspondence: fbernauer@geophysik.uni-muenchen.de

<sup>1</sup> Department für Geo- und Umweltwissenschaften, Ludwig-Maximilians-Universität München (LMU), 80333 München, Germany  
Full list of author information is available at the end of the article

example after meteorite or artificial impacts (Oberst and Nakamura 1991).

In November 2018, more than 40 years after the Apollo lunar missions, NASA's InSight (Interior exploration using Seismic Investigations, Geodesy, and Heat Transport) mission deployed a set of geophysical instruments on the surface of Mars. The InSight scientific payload includes the Seismic Experiment for Interior Structure (SEIS; Lognonné et al. 2019; Banerdt et al. 2020) that records seismic activity on Mars. Among the 174 seismic events recorded in less than 10 months after deployment, Giardini et al. (2020) identified two families of marsquakes: The majority are high-frequency events with energy content above 1 Hz. These events have small moment magnitudes ( $M_w < 3$ ), and are located close to the landing site. Their wavefields are supposed to travel as trapped waves within a low attenuating crust. Low-frequency events with energy content below 1 Hz have magnitudes of  $M_w = 3-4$ . These events are located below the crust and contain waves traveling inside the mantle. Using receiver function analysis, Lognonné et al. (2020) found a crustal layer with S-wave velocity between 1.7 and  $2.1 \text{ km s}^{-1}$  extending down to 8 and 11 km.

Investigating the interaction of the atmosphere with the ground, further reveals elastic properties of the subsurface (Sorrells 1971; Tanimoto et al. 2015). Lognonné et al. (2020) computed ground compliance from correlated pressure and deformation signals generated by closely passing convective vortices and provided depth dependent elastic properties in the vicinity of the lander. Atmosphere-ground interactions are often associated with ground tilt, which is an acceleration signal originating from rotational motions around a horizontal axis (Tanimoto and Valocin 2016; Garcia et al. 2020), and, for small rotation angles, is proportional to the horizontal angle of rotation. On the one side, this tilt contribution is another source of information on subsurface properties, on the other side, tilt contaminates acceleration recordings from inertial sensors (Crawford and Webb 2000; Bernauer et al. 2020). Panning et al. (2015) performed precise hypocenter localization using a terrestrial high quality single station data set as a proof of concept for event localization on Mars. Multiple orbit surface wave observations are a prerequisite for this approach. Given the fact that such observations are still missing in the InSight data set, up to now, event localization on Mars is only possible with highly uncertain assumptions on the interior structure (Khan et al. 2016; Giardini et al. 2020).

In the past years, seismology has seen substantial progress in extending the classic three-component ground motion observation concept to six-components (or 6 degrees-of-freedom, 6DoF), combining translational motion measurements with co-located observations

of three orthogonal components of rotational ground motions. The significance of this observational concept for seismic inverse problems and for the accuracy and consistency of ground motion measurements in general were extensively discussed in recent review papers, e.g., Igel et al. (2015) and Schmelzbach et al. (2018). The most important potential of the 6DoF concept for planetary exploration is the fact that 6DoF point measurements act like a small-scale seismic array returning wave field gradient information that is otherwise not accessible or associated with substantially more uncertainties when using only 3DoF of a single station.

Other approaches to constrain the interior structure of planetary objects use gravimetry and orbital observations (Kunze 1974; Talwani and Kahle 1976; McGovern et al. 2002; Kaspi et al. 2010; Huang and Wieczorek 2012; Konopliv et al. 2016). Such kind of observations suffer from relatively high errors on spacecraft orbit reconstruction especially for small objects like asteroids (Carroll and Faber 2018). On the other hand, rotation and orientation deduced from radioscience using a lander on Mars for instance and ground stations on Earth (Folkner et al. 2018) help determining interior properties.

A 6DoF motion sensor directly gives precise and reliable information on the lander trajectory before and after the rebounds. Biele et al. (2015) demonstrated that the landing and bouncing trajectory of Philae, part of the Rosetta Mission, on the surface of comet 67P/Churyumov-Gerasimenko (Ulamec et al. 2016) could be used to constrain a mechanical model of the surface layers at the landing site.

In this paper, we introduce novel and innovative approaches that help to better constrain the internal structure of planetary objects by including 6DoF instruments as scientific payload. These approaches include the concept of 6DoF seismology, the direct observation of a planetary object's rotational dynamics and its tides (schematically illustrated in Fig. 1), as well as the inertial observation of the full landing trajectory including rebounds and touchdown of a free falling lander. Within the project PIONEERS (Planetary Instruments based on Optical technologies for an innovative European Exploration using Rotational Seismology), an international collaboration develops 6DoF motion sensors dedicated to space sciences targeting the mentioned applications. The presented investigation is part of this project, funded by the Horizon 2020 research and innovation program of the European Commission. As a first step in establishing these methods in planetary sciences, we describe expected signals and their amplitude levels setting basic requirements for 6DoF sensor development for planetary exploration and give an outlook of what planetary exploration science can

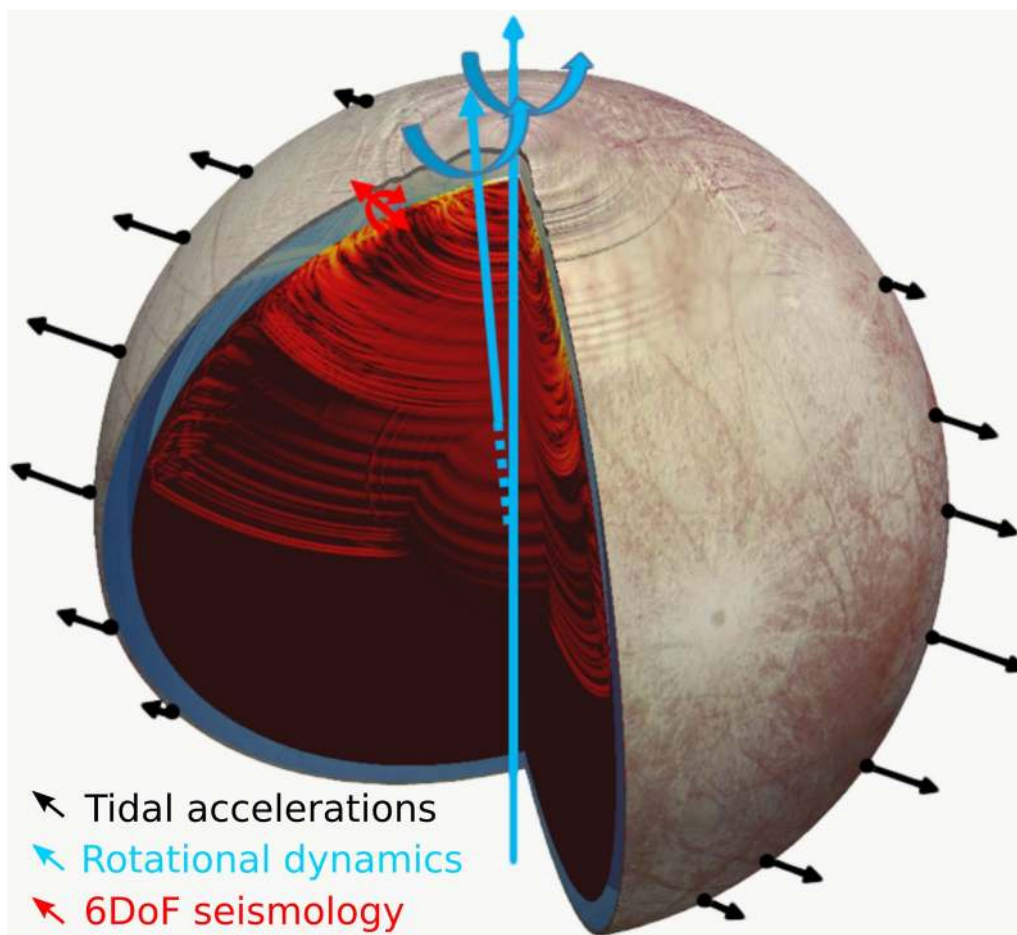


**Fig. 1** Schematic illustration of the phenomena to be observed with the PIONEERS instruments at one point at the surface of a celestial body. Ground motions during passage of a seismic wave field in 6DoF (red arrows) as well as rotational motions induced by the body’s rotational dynamics (e.g., librations, blue arrows) and translational motions induced by tidal forces (black arrows) are the target observables. Here, Jupiter’s icy moon Europa is shown as an example

expect from the deployment of high-precision 6DoF instruments by future space missions. We concentrate on the following set of potential target objects:

- *Dimorphos* The secondary body of the Earth-near binary asteroid system Didymos (officially named “(65083) Didymos I Dimorphos” by the International Astronomical Union) has a mean diameter of about 160 m. As the target of the NASA Double Asteroid Rejection Test (DART) mission (Cheng et al. 2016) and the associated post-impact survey mission Hera (Michel et al. 2018), it is of special interest for planetary defense applications.
- *Phobos* The innermost satellite of Mars has a tri-axial shape of 13.0 km × 11.4 km × 9.1 km in radius (Willner et al. 2010; Hurford et al. 2016). It is the target of the Japanese sample return mission named Martian Moons eXploration (MMX; Kuramoto et al. 2017) that aims at revealing the mysterious origin of Phobos.
- *Europa* Jupiter’s icy moon Europa has a radius of 1560.8 km. As a potentially habitable world, future lander missions to Europa would offer a unique opportunity to confirm the existence of liquid water within and below Europa’s icy shell as well as to characterize the sub-surface ocean (Pappalardo et al. 2013).
- *The Moon* The Earth’s satellite has a radius of 1737.4 km. The European Space Agency (ESA) recently published its priorities for scientific activities at the Moon in the next 10 years. Among those are the detection and characterization of polar water ice as well as the deployment of geophysical

instruments and the build-up of a global geophysical network (ESA 2019).

- *Mars*: the outer neighbor of our Earth has a radius of 3389.5 km. Since November 2018 the NASA InSight lander has been delivering a unique geophysical data set. The mission goals are to determine the interior structure, composition and thermal state of Mars, as well as to constrain present-day seismicity and impact cratering rates (Banerdt et al. 2020).

The project sets the basic scientific requirements for the 6DoF instruments developed within the framework of PIONEERS

### Instruments and technologies

For 6DoF motion observation in space sciences, we consider a combination of fiber-optic gyroscopes (FOG), micro-electro-mechanical systems (MEMS) and a very-broad-band seismometer (VBB) with optical readout.

*Fiber-optic gyroscopes* have the potential to measure rotational motions within a broad frequency range with a high dynamic range. Their measurement principle is based on the Sagnac effect (Laue 1911; Sagnac 1913), and exploits the difference between the optical path length of two counter propagating beams in a rotating optical fiber loop. These instruments are widely used as rotation rate sensors in gyro compasses or inertial measurement units for applications in inertial navigation (e. g. Lefèvre 2014). Recently, the first fiber-optic gyroscope especially designed for the needs of rotational seismology became commercially available (blueSeis-3A by iXblue, France, Bernauer et al. 2018). State-of-the-art fiber-optic gyroscopes use an optical fiber of several hundreds of meters length  $L$  that is wound up to a coil of diameter  $D$ . The scale factor, which determines the theoretical sensitivity of a fiber-optic gyroscope is directly proportional to the product of  $(L \cdot D)$ . Thus, the sensitivity of a fiber-optic gyroscope is a result of a trade-off between the dimensions of the coil, on one side, and geometrical stability and portability, on the other side. A portable sensor like the blueSeis-3A has a coil diameter in the order 0.25 m and needs a fiber length of about 6 km to reach a sensitivity level of  $20 \text{ nrad s}^{-1} \text{ Hz}^{-1/2}$  in a frequency range from 0.01 to 100 Hz. Table 1 lists self-noise levels and coil diameters of other fiber-optic gyroscopes currently used in seismology and inertial navigation.

*Micro-electro-mechanical systems* (MEMS) are widely used for acceleration sensing in a huge variety of applications ranging from strong-motion or engineering seismology to inertial navigation. MEMS are relatively small (in the range of millimeters to a few centimeters) electronic components that combine logical circuits and mechanical structures on a single chip and combine

**Table 1 Typical self-noise levels (SNL), and coil-diameters (D) of state-of-the-art fiber-optic gyroscopes**

	SNL ( $\text{nrad s}^{-1} \text{ Hz}^{-1/2}$ )	D (m)
FARO	6	0.75
blueSeis-3A	20	0.25
FOSREM	100	0.3
PHINS (FOG)	600	0.15
IMU50 (FOG)	1500	0.1

Self-noise levels are given for a frequency range from 0.01 to 100 Hz. The levels are reported for a single vertical component giant FOG FARO from Streckeisen, Switzerland, a blueSeis-3A from iXblue, France, a single component FOG FOSREM from Elproma Elektronika, Poland, and two navigation-grade fiber-optic gyros as parts of 6DoF North-seeking gyros (PHINS and IMU50 from iXblue, France)

**Table 2 Typical self-noise levels (SNL) in the corresponding frequency range for state-of-the-art MEMS accelerometers**

	SNL ( $\mu\text{m s}^{-2} \text{ Hz}^{-1/2}$ )	Frequency range (Hz)
SP (InSight)	< 0.01	0.01 – 10
EpiSensor ES-T	0.6	0.1 – 100
PHINS (ACC)	40	0.1 – 100
iXal A5	50	DC – 1000
IMU50 (ACC)	600	1 – 100

The levels are reported for the short-period instrument on the InSight Mission (SP), a typical strong-motion accelerometer commonly used in seismology (the EpiSensor ES-T from Kinemetrics, USA), and two navigation-grade accelerometers as parts of 6DoF freedom North-seeking gyros (PHINS and IMU50 from iXblue, France). The Quartz Vibrating Beam accelerometer iXal A5 from iXblue, France is the basis for PIONEERS compact sensor

advantages such as low power consumption, compact design and robustness. For example, the short-period (SP) sensors on the InSight mission have a self-noise level lower than  $10 \text{ nms}^{-2} \text{ Hz}^{-1/2}$  in a frequency range from 0.01 Hz to 10 Hz and are sufficiently robust to survive launch and landing (Lognonné et al. 2019). Table2 shows sensor self-noise levels and bandwidth of some MEMS accelerometers commonly used in seismology and inertial navigation.

*Very Broadband Seismometers* (VBB): Highly sensitive broadband recording of ground movement with an inertial sensor is only possible with a band-pass response in terms of acceleration, which avoids saturation of the system in presence of impulsive disturbances as well as long period thermal drifts or tilt (Wielandt 2012). In one of the most precise and thus extensively used seismometers for applications on Earth, the STS2 seismometer (by Streckeisen, Switzerland), this is realized using the so-called force-balance feedback circuit, which compensates the inertial force with an electrically generated force so that the seismic mass itself moves as little as possible.

The principle of VBB force-balanced feedback combined with extremely sensitive transducers extends the bandwidth of an inertial sensor keeping sensor self-noise low at the same time. The STS2 has a flat velocity response from 0.001 to 30 Hz and a self-noise level lower than  $10^{-9} \text{ ms}^{-2} \text{ Hz}^{-1/2}$  (Streckeisen 1995). Another way of extending the bandwidth of an inertial sensor is to use optical read out devices based on the principles of laser interferometry to track the position of the seismic mass. Berger et al. (2014) compared such a system to a standard STS2 seismometer and a superconducting gravimeter located in the Black Forrest Observatory, Germany. They reached promising noise levels comparable to those of the STS2 and the gravimeter in a very broad frequency range from some  $\mu\text{Hz}$  to 100 Hz.

To cover a wide range of applications, within the framework of the PIONEERS project, two sensor types are developed: three orthogonally aligned Quartz Vibrating Beam accelerometers based on MEMS technology (type: iXal A5 by iXblue, France) and three orthogonally aligned FOGs share the same housing in the so-called PIONEERS compact model. This inertial measurement unit should fit approximately 3 Cubesat units and reach a high technology readiness level (TRL 6). We target self-noise levels of  $20 \mu\text{ms}^{-2} \text{ Hz}^{-1/2}$  and  $2 \mu\text{rads}^{-1} \text{ Hz}^{-1/2}$  in a frequency range from 0.01 Hz to 400 Hz. The PIONEERS high-performance prototype sensor combines a VBB seismometer with optical readout for measuring translational motions and a giant fiber-optic loop for rotation rate sensing with a diameter in the order of 0.5 m to 1 m. We target self-noise levels of  $10 \text{ pms}^{-2} \text{ Hz}^{-1/2}$  and  $5 \text{ nrads}^{-1} \text{ Hz}^{-1/2}$  in a frequency range from 0.001 Hz to 10 Hz.

### Applications and expected signal ranges

Future space missions carrying, for example, one of the PIONEERS 6DoF motion sensing instruments can benefit from an enhanced scientific output by including the complete observation of the full landing trajectory of a free falling lander, the direct observation of a planetary object's rotational dynamics, and the potentials of 6DoF seismology.

### Landing process and lander–surface interactions

In principle, as an inertial measurement unit, a 6DoF motion sensor can record specific force effects acting on a lander from its release from the mother spacecraft to its final rest on the surface of the target object. Such a measurement can address two scientific objectives:

- From the lander–surface interaction during rebounds, we can directly infer physical properties of the target object's surface material.

- Observing the lander trajectory during free-fall and in between rebounds, makes it possible to constrain the local gravity field of the target body.

In the following, we will derive expected signal levels and their frequency range as well as minimum and maximum signal amplitudes that a 6DoF sensor must resolve to be able to scientifically address the stated objectives. We will consider lander–surface interactions only for small body targets Dimorphos and Phobos for which landing is performed by a free-fall phase to the body allowed by the very low gravity accelerations and the subsequent low impact velocities, according to the current mission design state of the art. For planetary targets, the entry, descent and landing phase will be performed by using various thrusters and, if possible, parachute systems that will interfere with the landing acceleration and rotation measurements.

We will describe the signals in terms of translational acceleration and rotation rate and their amplitude spectral density (ASD). The maximum values of acceleration, rotation rate and the frequency range will be determined from the values expected during the lander–ground interactions. The minimum values of acceleration, rotation rate and frequency range will be determined from the accuracy needed to determine the impact angle of the lander at the first lander–ground interaction, and to infer the local gravity field from the reconstruction of the lander trajectory between rebounds.

### Surface properties

The signal levels we expect from the landing and touchdown, depend on the lander properties, especially mass and size of the lander. Only these two parameters are considered in this first estimate of accelerations and rotations experienced by the PIONEERS instrument. However, the full mass distribution inside the lander and the moments of inertia of the lander are formally required to have a full estimate of the acceleration and rotation experienced during lander–ground interactions. In the following estimates, the lander is assumed to be an aluminum cube of length  $a$  and mass  $m$  with a Young's modulus of 69 GPa and a Poisson ratio of 0.35. Two typical asteroid landers will be considered:

- A MASCOT (Mobile Asteroid Surface Scout)-like lander with  $a = 0.5 \text{ m}$  and  $m = 50 \text{ kg}$  as it is part of the JAXA Hayabusa2 probe (Ho et al. 2017).
- A 3-unit Cubesat-like lander with  $a = 0.3 \text{ m}$  and  $m = 5 \text{ kg}$ .

Lander–ground interactions during a rebound depend on several parameters: the ground and lander

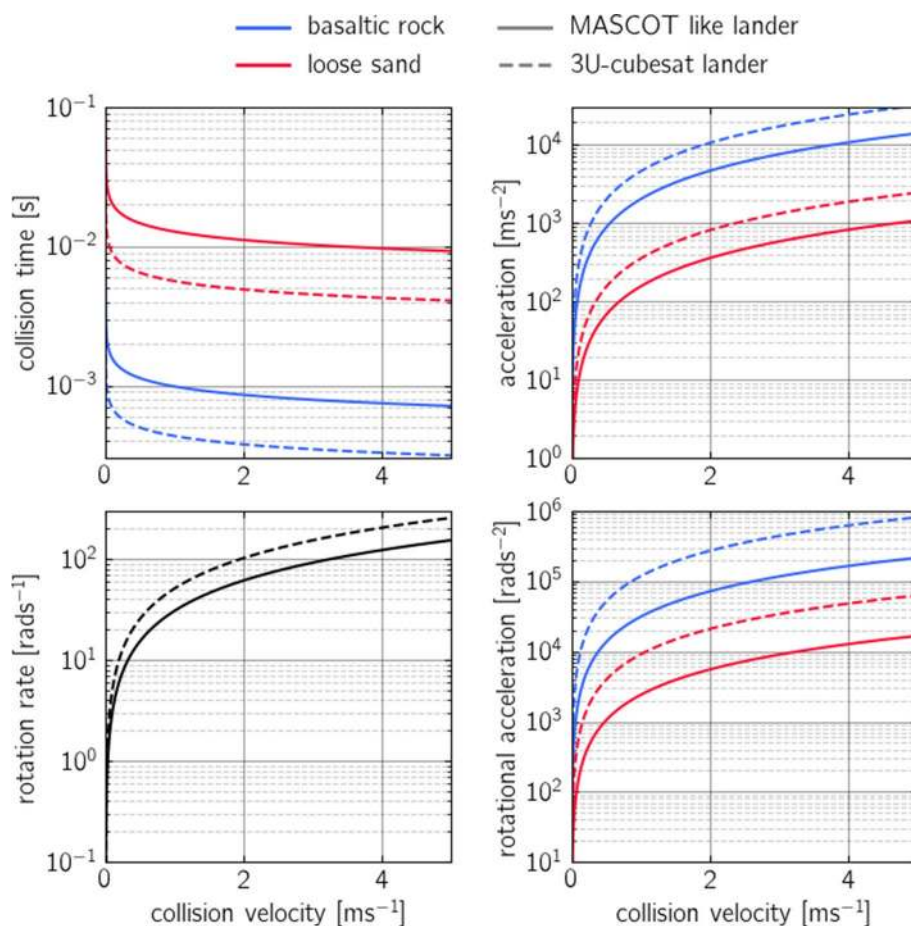


**Fig. 2** Lander–surface interaction. Estimated collision time (upper left), and the derived maximum transverse acceleration (upper right) for two different surface materials (loose sand and basaltic rock) as well as for two different lander types (a MASCOT-like lander and a 3-unit cubesat lander). Maximum rotation rate (lower left) and rotational acceleration (lower right) can be derived under assumption of total energy conservation

properties, the lander incident velocity  $v_i$  and impact angle, and the resulting coefficient of restitution ( $CoR$ , linked to all of the previous parameters). The ground parameters of the future target are generally unknown, hence the interest of such measurements.

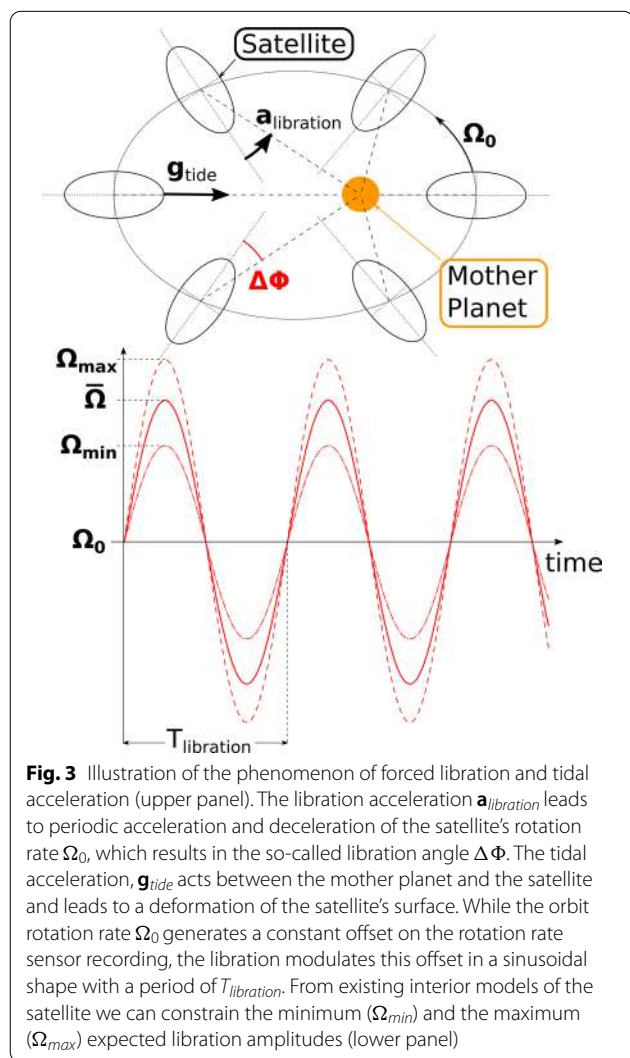
Here, we will consider two different material types (hard rock like basalt with a Young’s Modulus of 50 GPa and Poisson ratio of 0.3, and loose sand with a Young’s Modulus of 50 MPa and a Poisson ratio of 0.25). We present the acceleration and rotation rate amplitudes as a function of the lander incident velocity, which will depend on the deployment strategy. This strategy strongly depends on the escape velocity of the target. A conservative assumption is that the lander incident velocity will be smaller than half the escape velocity of the target body, thus smaller than  $5 \text{ ms}^{-1}$ , respectively,  $0.03 \text{ ms}^{-1}$ , for Phobos, respectively, Dimorphos. Moreover, personal discussion with MMX rover’s team

indicate that the incident velocity for that mission on Phobos will be smaller than  $1 \text{ ms}^{-1}$ .

In order to estimate maximum values of accelerations and rotations during the impact, we used the two following over-simplified assumptions. First, the  $CoR$  is set to its maximum value of 1 (velocity after rebound is equal and opposite to incident velocity). Then, the collision duration  $t_c$  is estimated with a simplified Hertzian mechanics assumption for elastic collisions (Fig. 2, upper left; Krijt et al. 2013). These two assumptions over-estimate the maximum accelerations and rotation accelerations felt by the lander (Goldman and Umbanhowar 2008; Murdoch et al. 2017), but are a good starting point to scale our instrument measurement range. Given our assumption that the  $CoR = 1$ , the absolute change in the velocity of the lander is then  $2v_i$ , and this occurs within the collision duration  $t_c$ . By using these values and the two lander types, we can estimate the

maximum translational acceleration experienced by the lander (Fig. 2, upper right).

In order to estimate the maximum rotation rate felt by the lander during the lander–ground interaction phase, we assume that the total kinetic energy ( $E_{kin}$ ) of the lander is conserved and that the resulting motion after rebound is purely rotational ( $E_{kin} = E_{rot} = 1/2I\omega^2$ , with the moment of inertia of the lander  $I$ , and the final rotation rate  $\omega$ , Fig. 2, lower left). Designing the sensor according to this extreme scenario, ensures that the sensor does not clip during touchdown and rebounds. For such kind of rotational sensors, the rotational acceleration can saturate the sensors, thus being a critical parameter. We estimate the maximum rotational acceleration by assuming that the maximum rotation rate is reached within the collision duration  $t_c$  (Fig. 2, lower right).



Finally, we estimate the maximum amplitude spectral density levels from the maximum (clip level) values assuming that these signals are generated at the highest possible frequency, that these signals have a bandwidth of 100 Hz, and that the clip level is 3 times above the root mean square of the signal.

**The local gravity field**

The local gravity field can be determined from the lander trajectory between rebounds. It requires the knowledge of the velocity vector after rebound, and the duration of flight in between two rebounds in addition to a local terrain model. The precision on the knowledge of the velocity vector depends on both the precision of the accelerations and rotations during the rebound phase. In the case of Phobos, assuming that the lander minimum incident velocity is  $0.05 \text{ ms}^{-1}$  and a minimum CoR of 0.1, the rebound velocity is  $5 \text{ mms}^{-1}$ . The precision of the local gravity estimate depends linearly on the precision of the retrieval of the velocity component in the direction of local gravity field just after rebound. Assuming we would like to determine the local gravity better than 1%, this imposes a precision on the velocity after rebound of  $0.05 \text{ mms}^{-1}$ . For a worst case value of collision time of 1 ms, this implies a precision on the acceleration measurements of  $0.05 \text{ ms}^{-2}$  at about 1000 Hz. In the case of Dimorphos, because the escape velocity is 50 to  $100 \text{ mms}^{-1}$ , the incident velocities for landing will be on the order of  $10 \text{ mms}^{-1}$ , thus putting a precision on the acceleration measurements of about  $0.01 \text{ ms}^{-2}$  at about 1000 Hz.

The impact angle of the lander is an important parameter for further interpretation of the impact. In order to determine the impact angle of the lander, assuming a known orientation during the release by the mother spacecraft, a digital terrain model of the impact location is required. Determining the impact angle with a precision of  $1^\circ$ , which is in the order of the typical precision of terrain slope and tilt derived from digital elevation models (Bolstad and Stowe 1994; Barnouin et al. 2020), requires a precision of  $1^\circ \text{h}^{-1}$  on the rotation speed measurement (which is approximately  $5 \mu\text{rads}^{-1}$ ), assuming a free-fall phase of maximum one hour. These rotation rates are expected to be observed at low frequencies, and a typical minimum expected frequency of 1 mHz can be considered.

**Rotational dynamics and tidal accelerations**

In this section, we consider the rotations of planets, moons, and other bodies of the Solar System and their possible variations. Usually, the rotation of a planet or a moon or an asteroid is approximately uniform, meaning

that the object rotates with an almost constant rate. Small variations in the rotation rate occur due to various reasons. For the icy satellites or asteroid binary systems, the largest rotation variations are due to the gravitational torque exerted by the mother planet, or the central asteroid. The central body exerts a gravitational torque on the non-spherical satellite, which therefore accelerates or decelerates its rotation depending on its orientation with respect to the central body, causing the so-called forced librations (see Fig. 3, upper panel). The amplitude of the forced libration depends on the equatorial flattening of the satellite, the semi-major axis and eccentricity of the orbit, the mass of the mother planet, and on the interior structure and mass distribution of the satellite in particular. Therefore, observing these rotational variations or librations allows constraining the interior properties of a body.

Forced librations cause a sinusoidal modulation of the satellite's rotation around the mother body with the period of the libration ( $T_{libration}$ ) and the libration angle  $\Delta\Phi$  as amplitude (see Fig. 3, upper panel). With a rotation rate sensor we expect to observe a signal  $\bar{\Omega}$  that is the sum of the orbit rotation rate  $\Omega_0$  and the rotation rate induced by libration:

$$\bar{\Omega} = \Omega_0 \left( 1 + \frac{\Delta\Phi \cos(\Omega_0 t)}{2\pi} \right). \quad (1)$$

Here, we assume a 1:1 spin-orbit coupling, where the libration period is equal to the primary orbit period,  $T_0 = 2\pi/\Omega_0 = T_{libration}$ . With a given set of interior models of a planetary object or an asteroid, we can define a range of expected libration angles from  $\Delta\Phi_{min}$  to  $\Delta\Phi_{max}$ . Using Eq. (1) with  $\Delta\Phi_{min}$  and  $\Delta\Phi_{max}$ , we can define a minimum and a maximum rotation rate expected from librations ( $\Omega_{min}$  and  $\Omega_{max}$  in Fig. 3, lower panel). With the libration rotation rate measurement, we want to set further constraints onto the interior model of a planet or asteroid. Therefore the precision,  $p$ , of the rotation rate measurement has to be better than a certain percentage of the range between  $\Omega_{min}$  and  $\Omega_{max}$ . Here, we set this percentage to 10% and  $p = 0.1(\Omega_{max} - \Omega_{min})$ . In order to make this precision comparable to sensor self-noise levels in terms of amplitude spectral density, we estimate the required level of precision as  $P_{ASD} = p\sqrt{T/2}$ , where  $T$  is the measurement duration estimated as  $T = 10T_{libration}$ . This level of precision is approximately equivalent to the maximum acceptable self-noise level the sensor must show within a frequency band of 1/3-octave centered around the frequency of libration ( $f_{libration} = 1/T_{libration}$ ) to be able to measure the expected libration rotation rate with the required precision (see e.g., Bormann and Wielandt (2013) for details on the approximate conversion between measured amplitudes and spectral densities).

For the terrestrial planets with an atmosphere (e.g., Earth, Mars, Venus), the largest changes of the primary orbit rotation rate are due to the atmosphere dynamics and angular momentum exchange between the solid planet and the atmosphere, the so-called length-of-day (LOD) variations. Directly observing LOD variations with a suitable rotational motion sensor, helps constraining the integral state of the atmosphere and its interaction with the solid planet.

The acceleration signal,  $g_{tide}$  observed with a sensor, for example the PIONEERS optical VBB, on the surface of a body that undergoes the gravitational effect of the mother body, consists of the direct tidal attraction,  $g_{direct}$ , the acceleration of the surface related to the radial displacement involving Love number  $h$  and the effect of the mass redistribution due to the tides related to Love number  $k$ :

$$\begin{aligned} g_{tide} &= \delta g_{direct} \\ &= \delta \frac{GM_{parent} r}{d^3}, \end{aligned} \quad (2)$$

where  $M_{parent}$  is the mass of the mother body,  $d$  is the distance between the two bodies,  $r$  is the radius of the satellite body and  $G$  is the gravitational constant.  $\delta = 1 + h - \frac{3}{2}k$  is the so-called tidal gravimetric factor. With a given set of interior models of a planetary object or an asteroid, we can constrain a range of expected tidal gravimetric factors from  $\delta_{min}$  to  $\delta_{max}$ . Using Eq. (2) with  $\delta_{min}$  and  $\delta_{max}$ , we can define a range of expected tidal accelerations that has to be observed with a precision  $p = 0.1(g_{tide,max} - g_{tide,min})$ . In order to make this precision comparable to sensor self-noise levels in terms of amplitude spectral density, we proceed in an equivalent way as for the librations. We estimate the required level of precision as  $P_{ASD} = p\sqrt{T/2}$ , where  $T$  is the measurement duration estimated as  $T = 10T_{tide}$  and  $T_{tide}$  is the tidal period.

In the following, we will report minimum and maximum signal amplitudes and required measurement resolutions for libration rotation rates and tidal accelerations as they are expected on Dimorphos, Phobos, Europa, the Moon and Mars.

### Dimorphos

The rotation dynamics of the binary asteroid system Didymos are particularly important due to the studies that will be induced by the DART (double asteroid redirection test) impact on the secondary body in 2022. According to Richardson et al. (2016), Dimorphos will probably show free librations that may range from 0.2 to 1.5 h in terms of rotation period. Even without the DART impact, there is a forced libration at the exact period of the secondary asteroid orbital period of 11.9 hours. The amplitude of the forced libration depends on many



parameters such as the interior mass distribution or the geometry of the orbit of Didymos secondary with respect to the primary asteroid. For different possible interior models, the amplitudes reach a range of libration angles from  $6^\circ$  to  $45^\circ$  (Naidu and Margot 2015; Michel et al. 2018). Using Eq. (1), we end up with a minimum expected rotation rate amplitude of  $152 \mu\text{rads}^{-1}$  and a maximum of  $161 \mu\text{rads}^{-1}$ . The noise level of the measurement must be lower than  $0.41 \text{ mrad s}^{-1} \text{ Hz}^{-1/2}$  at a frequency of  $23 \mu\text{Hz}$ .

### Phobos

A variety of models exist of the interior of the Martian moon Phobos. They include rubble pile models heavily fractured and porous compressed models or models containing evenly distributed ice in the volume (Le Maistre et al. 2019). This range of models leads to an expected libration amplitude of  $-1.2^\circ$  with an uncertainty of  $0.15^\circ$ . This uncertainty corresponds to a range of forced libration rotation rates from  $228 \mu\text{rads}^{-1}$  to  $229 \mu\text{rads}^{-1}$ . In order to resolve this range with the required accuracy, the sensor self-noise level must be lower than  $23.5 \mu\text{rads}^{-1} \text{ Hz}^{-1/2}$  at  $36 \mu\text{Hz}$ . The tidal accelerations associated with different interior models are around  $0.57 \text{ mms}^{-2}$  and require a maximum sensor self-noise level better than  $5.4 \text{ nms}^{-2} \text{ Hz}^{-1/2}$  at  $36 \mu\text{Hz}$ .

### Europa

Europa has librations forced by Jupiter. The amplitudes of these librations are changing with the ice shell thickness. For Europa's main libration with a period of 3.52 days, Van Hoolst et al. (2013) have derived a range of amplitudes from 105 to 165 m on the equator at the surface from realistic models of Europa's interior. This range corresponds to minimum and maximum expected rotation rate amplitudes of  $491.7 \mu\text{rads}^{-1}$  and  $492.1 \mu\text{rads}^{-1}$ , respectively, and results in a required sensor self-noise level of  $12.3 \mu\text{rads}^{-1} \text{ Hz}^{-1/2}$  at  $78 \mu\text{Hz}$ . The tidal accelerations associated with different interior models are:  $0.7 \text{ mms}^{-2}$  and  $1.3 \text{ mms}^{-2}$  for the minimum and maximum values, which results in a required maximum sensor self-noise level of  $14.3 \text{ mms}^{-2} \text{ Hz}^{-1/2}$  at  $78 \mu\text{Hz}$ .

### The Moon

Librations of the Moon are already very well known. The forced libration at the Moon rotation period is at the spin-orbit frequency with an amplitude of about 16.8 arcsec inversely proportional to the mantle moment of inertia  $C_m$  known at the third decimal [ $C_f/C = 0.0012 \pm 0.0004$ , where  $C_f$  is the fluid core moment of inertia and  $C$  the total moment of inertia  $C = C_f + C_m$ ; see Rambaux and Williams (2011)]. The liquid core effects on the libration are already seen with

the method of lunar laser ranging (LLR). The remaining uncertainty on the libration is thus very small requiring a precision of the measurement of  $37.9 \text{ prads}^{-1} \text{ Hz}^{-1/2}$  at a frequency of  $0.4 \mu\text{Hz}$ . Tides, on the other hand, range from  $14.49$  to  $14.51 \text{ mms}^{-2}$ , setting a required maximum sensor-self-noise level of  $6.3 \mu\text{ms}^{-2} \text{ Hz}^{-1/2}$  at a frequency of  $0.4 \mu\text{Hz}$ .

### Mars

Mars undergoes length-of-day variations (LOD) induced by the atmosphere. The  $\text{CO}_2$  global cycle, the mass exchange between the atmosphere and the polar ice caps and winds are the major contributors to the LOD variations. Also the dust content of the atmosphere can change the LOD, which cannot be forecast. Van den Acker et al. (2002) estimate a total annual LOD variation of 0.253 ms, which corresponds to a variation in the rotation rate of  $2.7 \text{ prads}^{-1}$ . The tidal accelerations associated with different interior models are:  $40.02 \text{ nms}^{-2}$  and  $40.50 \text{ nms}^{-2}$  for the minimum and maximum values, requiring a maximum sensor self-noise level of  $1.4 \mu\text{ms}^{-2} \text{ Hz}^{-1/2}$  at a frequency of  $17 \text{ nHz}$ .

### 6DoF seismology

For the purpose of constraining the interior structure of a planetary body, the concepts of seismology play a major role. On Earth, recent studies have shown vital advantages of 6DoF observations compared to the classical 3DoF approach (Wassermann et al. 2016; Sollberger et al. 2018; Schmelzbach et al. 2018; Wassermann et al. 2020; Bernauer et al. 2020; Yuan et al. 2020). Among the major advantages for planetary applications are the following:

- Wassermann et al. (2016) and Keil et al. (2020) demonstrated the possibility of estimating surface wave phase velocity profiles of the upper few 100 m using ambient noise recordings with a single station 6DoF point measurement.
- Hadziioannou et al. (2012), Wassermann et al. (2020) and Yuan et al. (2020) demonstrated accurate estimation of source direction using either a combination of transverse acceleration and vertical rotation rate or both horizontal rotation rate components from a single point measurement.
- Donner et al. (2017) and Schmelzbach et al. (2018) demonstrated ways to estimate hypocenter locations from single station 6DoF observations.
- Due to the fact that measuring rotations can be understood as measuring the curl of the wavefield, rotational motion measurements can provide a direct estimate of the S-wave component of the wavefield. Sollberger et al. (2016) computed array-derived rota-

tion from Apollo 17 active seismic experiment data. This enabled to identify S-wave arrivals and to construct an S-wave velocity profile of the shallow lunar crust.

- Sollberger et al. (2018) present a fully automated way, to separate the seismic wavefield into its different wave modes using only one single 6DoF recording station and apply the method to remove surface wave energy while preserving the underlying reflection signal.
- Seismometer recordings from strong ground motions and long period ground motions can be severely contaminated by tilt–horizontal coupling. Direct observation of pure rotational ground motion makes it possible to correct for the contribution of dynamic tilt in translational acceleration recordings (Bernauer et al. 2020).
- Results from numerical studies strongly indicate that seismic source inversion benefits from including observations of rotational ground motions. The gradient information contained in the rotational motion records significantly reduces non-uniqueness in finite source inversions and increases the resolution of moment tensor inversion (Bernauer et al. 2014; Reinwald et al. 2016; Donner et al. 2016).

In the following, we provide amplitude levels expected from seismic signals of various origins. Only the Apollo 17 active seismic experiment data set provides us with the opportunity to directly estimate rotation rates from a small-scale seismic array. For all other cases, we estimate rotation rate amplitudes by dividing the translational acceleration with the estimated surface wave phase velocity. Though this procedure is only valid for plane wave propagation, we regard it as a proper way to estimate rotation rate signal levels for 6DoF sensor design for future space missions relying on 6DoF seismic exploration.

#### ***Dimorphos and Phobos***

Asteroids are supposed to be seismically active bodies (Murdoch et al. 2015). Murdoch et al. (2017) propose expected seismicity models for Dimorphos considering seismogenic sources such as meteoroid impacts, tidal stress changes and thermal cracking. Based on four different interior models (a consolidated body with constant density and seismic velocities, a layered body consisting of a homogeneous consolidated body covered with a regolith layer of a globally constant thickness of 1 m and 10 m, and a macro-porous internal structure model including voids extending to the deep interior) they compute amplitude spectral densities from a signal generated

by a meteoroid impact recorded in a range of distances from  $1^\circ$  to  $180^\circ$ . The signal levels of a meteoroid with a mass of 1 mg impacting with a velocity of 6 km/s is between  $10^{-10}$  and  $10^{-1} \text{ ms}^{-2}\text{Hz}^{-1/2}$  within a frequency range from 1 Hz to  $10^3$  Hz. In general, we expect signal levels from natural impacts on small bodies to be comparable to those measured on the Moon. Due to higher temporal thermal gradients, signals originating from thermal cracking are expected to be slightly larger on Dimorphos than on the Moon (Murdoch et al. 2017). The seismic moment from an event generated by tidal forcing may be described by the same equations as for thermal cracking (as described in Delbo et al. (2014), thermal fatigue, a mechanism of rock weathering and fragmentation, is predicted to occur on asteroid surfaces). Therefore we expect the signal levels and frequency ranges from tidal events to be similar to those from thermal cracks. Taking into account the impact of the DART spacecraft in 2022 on Dimorphos, we also consider artificial impacts and active sources to produce signals in a future seismic asteroid mission. These signals are likely to match the observations from the Moon in terms of acceleration spectral density. For the estimation of rotation rate levels, we assume a surface wave phase velocity in the order of  $100 \text{ ms}^{-1}$  in the upper regolith layer.

#### ***Europa***

Expected seismicity on Jupiter's icy moon Europa was extensively studied by Lee et al. (2003); Panning et al. (2006); Vance et al. (2018) and Stähler et al. (2018). Signals carrying energy at frequencies above 1 Hz are expected from surface ice cracking or meteoroid impacts. In order to access ground motion levels from ambient seismic noise, Panning et al. (2018) generated seismicity catalogues based on a Gutenberg–Richter relationship constrained by a cumulative moment release and a maximum event size. Four different seismicity models were combined with five structural models of Europa's interior to simulate the seismicity level and wave propagation on Europa. Seismic background noise on Europa covers a wide frequency range from 0.001 Hz to 10 Hz. On the basis of this seismicity model, Panning et al. (2018) estimate ground acceleration amplitudes for an  $M_w 3.1$  event in  $90^\circ$  distance to the receiver. Signal amplitude levels are expected between  $10^{-10} \text{ ms}^{-2}\text{Hz}^{-1/2}$  and  $10^{-7} \text{ ms}^{-2}\text{Hz}^{-1/2}$  below 1 Hz. Panning et al. (2006) estimates the acceleration generated by the free oscillating normal mode  ${}_0S_2$  excited by a  $M_w 5$  event in the range of  $10^{-12} \text{ ms}^{-2}$  with a dominant frequency of approximately 0.1 mHz depending on the thickness of the ice shell. For the estimation of rotation rate levels, we assume a surface wave phase velocity of  $1000 \text{ ms}^{-1}$ .

### The Moon

Signal levels of moonquakes and meteoroid impacts on the Moon are derived from Apollo data. According to Lamlein (1977), 90% of ground motion signals recorded with the Apollo instruments do not exceed peak to peak amplitudes of 10 DU (Digital Units). Using recently revised transfer functions of the Apollo instruments (Nunn et al. 2020) 10 DU correspond to a ground acceleration of about  $10 \text{ nms}^{-2}$  (taking the mid-period instrument transfer function as a basis). The maximum amplitudes of observed thermal moonquake signals are in the order of  $2.4 \mu\text{ms}^{-2}$  at 10 Hz (Duennebieer and Sutton 1974; Murdoch et al. 2017). So-called thermal micro-cracks are strongly related to the lunation period and build the major contribution to the seismic background signal (Sens-Schönfelder and Larose 2010). These signals reach acceleration amplitudes in the range from  $40 \text{ nms}^{-2}$  to  $400 \text{ nms}^{-2}$  at 10 Hz (Murdoch et al. 2017). Deep moonquakes exhibit tidal periodicity and are thought to be linked to tidal stress changes. These events only rarely exceed magnitudes corresponding to a terrestrial body wave magnitude  $m_b$  2.5 (Frohlich and Nakamura 2009) and show amplitudes in the range of several  $\text{nms}^{-2}$ .

Natural impacts are among the largest signals in the Apollo data. Depending on source receiver distance and impactor mass, amplitudes in the range of  $0.1 \mu\text{ms}^{-2}$  can be reached in a frequency range from 1 to 100 Hz.

In addition, we derived signal levels for rotation rate and translational acceleration for artificial impacts and explosions from the Apollo 17 active seismic experiment. First, the geophone data was converted from digital units to ground velocity (Nunn et al. 2020). Then, rotation rates were estimated by an inversion of the array data for the spatial gradients of the velocity field (Spudich et al. 1995; Sollberger et al. 2016). As an example, Fig. 4 shows a translational acceleration signal recorded after the detonation of 454 g of explosive in a distance of 1.2 km from the Apollo 17 geophone array. The bottom panel of Fig. 4 shows the corresponding array-derived rotation rate. The signals were bandpass-filtered between 3 Hz and 7 Hz. Artificial impacts and explosions reach translational acceleration amplitude levels between  $1 \mu\text{ms}^{-2}\text{Hz}^{-1/2}$  and  $1 \text{ mms}^{-2}\text{Hz}^{-1/2}$  as well as rotation rate amplitude levels between 0.1 and  $10 \text{ mrad s}^{-1}\text{Hz}^{-1/2}$  in a frequency range from 1 to 100 Hz. For thermal quakes, deep moonquakes and natural impacts we estimated rotation rate amplitudes by assuming a surface wave phase velocity of  $100 \text{ ms}^{-1}$  in the upper regolith layer.

### Mars

As we can observe in the NASA InSight Discovery mission SEIS data (Banerdt et al. 2020) one major contributor to the budget of seismic signals on Mars is its atmosphere (Giardini et al. 2020; Lognonné et al. 2020).

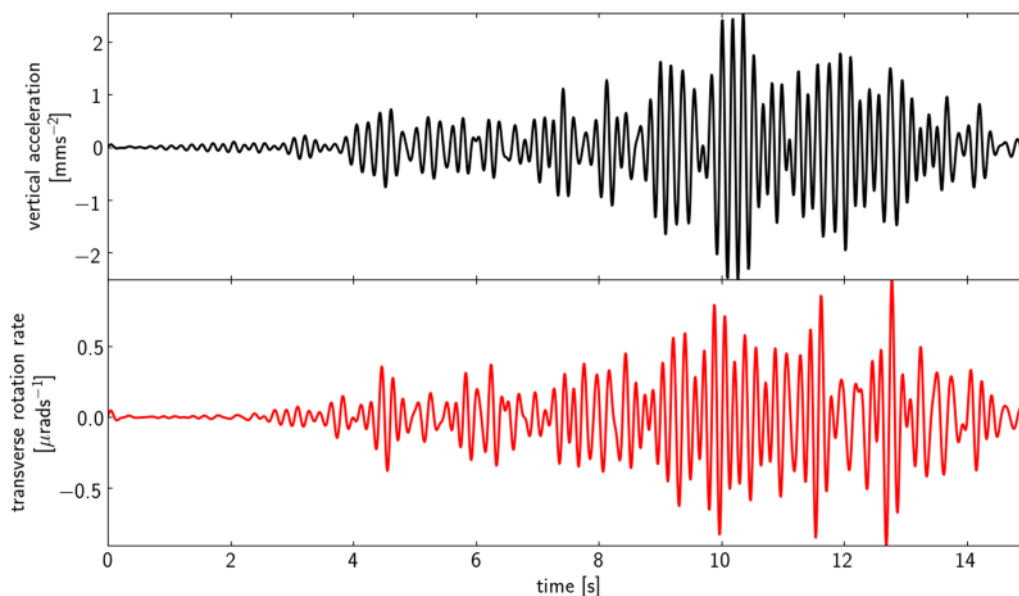


**Fig. 4** Active seismic signals on the moon. Translational acceleration signal recorded after the detonation of 454 g of explosive in a distance of 1.2 km from the Apollo17 geophone array (top panel) and the corresponding array-derived rotation rate (bottom panel), bandpass-filtered between 3 and 7 Hz

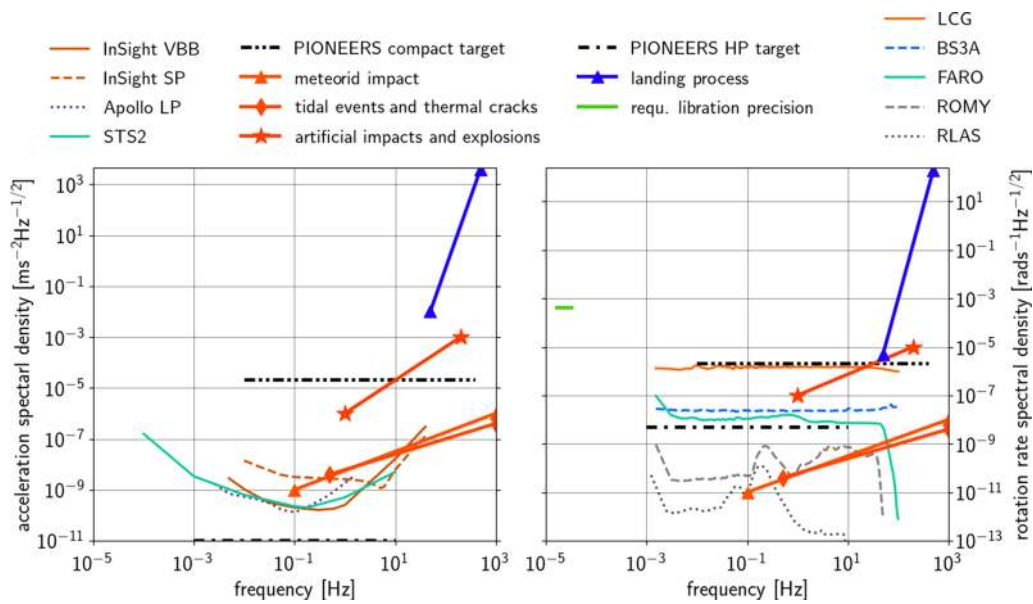


**Fig. 5** Expected signal levels on Dimorphos. For forced librations, the required resolution is shown. Additionally, self-noise levels of commonly used sensors are shown: Left panel: Very broad band (VBB) sensor and short-period (SP) sensor on the InSight mission (Lognonné et al. 2019), the long-period (LP) instrument from the Apollo mission (Nunn et al. 2020), and an STS2 (Sleeman and Melichar 2012). Right panel: LCG-Demonstrator from Litef, Germany (Bernauer et al. 2012), BlueSeis3A from iXblue, France (Bernauer et al. 2018), and the giant fiber-optic gyroscope FARO (by Streckeisen). We also show ambient noise recordings from large ring-laser gyroscopes RLAS located in Wettzell, Germany and ROMY located in Fürstenfeldbruck, Germany

Atmospheric pressure variations including small-scale convective vortices as well as large scale atmosphere dynamics pressure perturbations moving with the wind

and gravity waves, interact with Mars’ surface producing horizontal ground rotation (tilt). Using the theory of Sorrells (1971) and assuming that rotations are

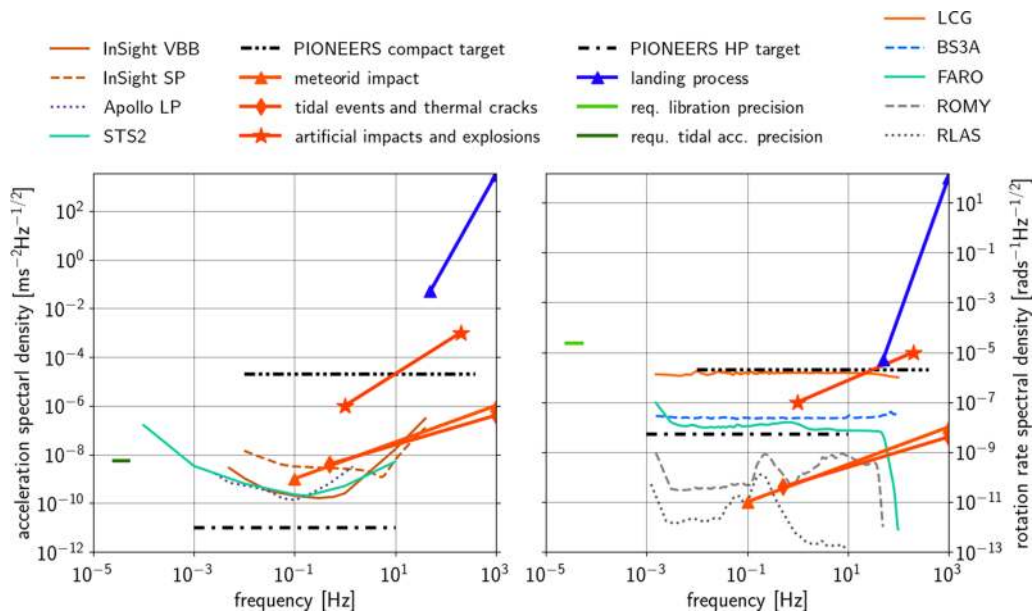
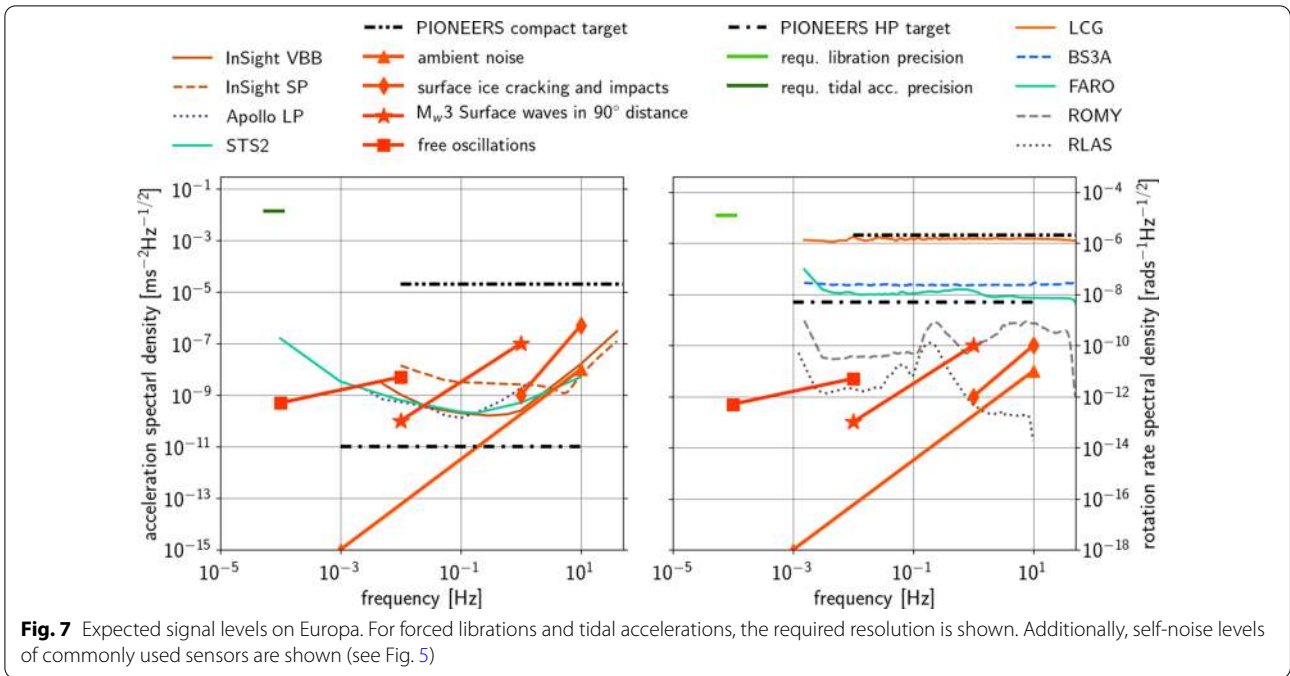
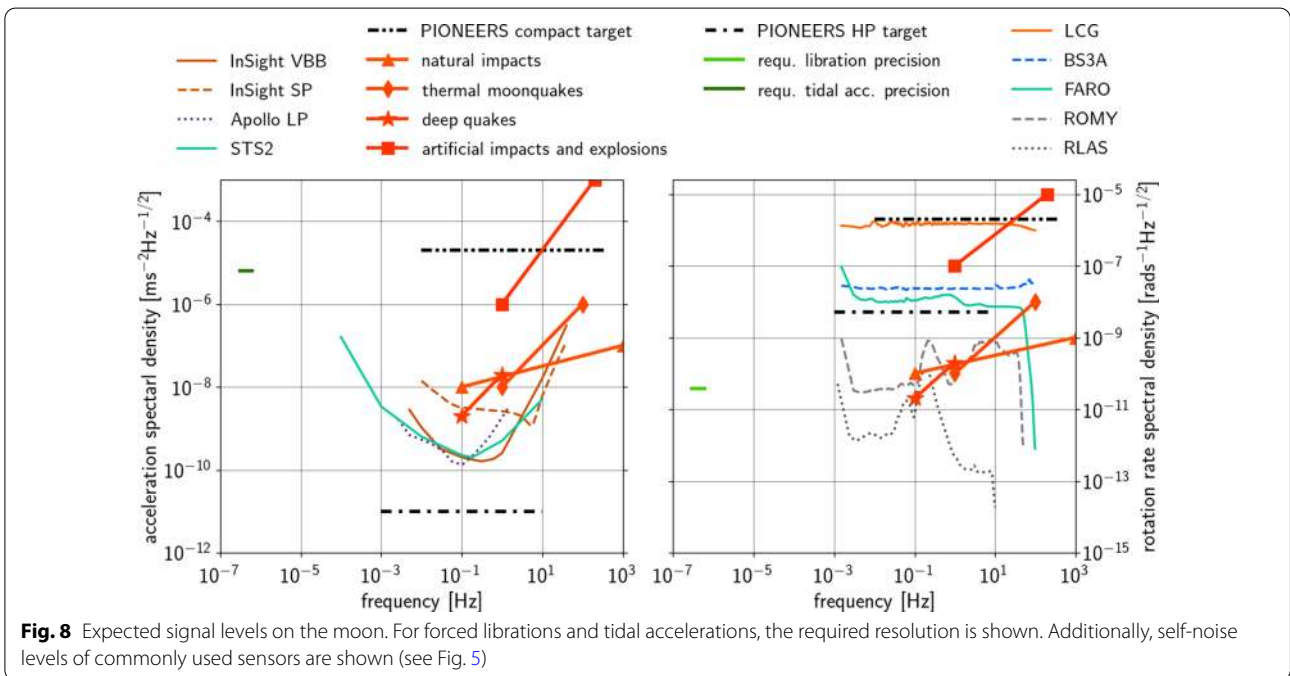


**Fig. 6** Expected signal levels on Phobos. For forced librations and tidal accelerations, the required resolution is shown. Additionally, self-noise levels of commonly used sensors are shown (see Fig. 5)



induced by plane pressure waves, we can compute rotation rates expected from atmosphere ground coupling for a simplified case sub-surface structure (homogeneous sub-surface model with Poisson ratio of 0.25 and a Young’s modulus of 900 MPa) and end up with rotation rate levels from 1 prads<sup>-1</sup>Hz<sup>-1/2</sup> to 0.1 nrad<sup>-1</sup>Hz<sup>-1/2</sup> for frequencies between 0.01 Hz and 1 Hz. The

accelerations induced by atmospheric pressure changes and dust devils are straight forward to estimate because they dominate the signal of SEIS-InSight instrument. Garcia et al. (2020) report acceleration amplitude levels ranging from 0.1 to 1 μms<sup>-2</sup>Hz<sup>-1/2</sup> for frequencies between 0.01 Hz and 1 Hz. Maximum amplitude values for signals from ground atmosphere coupling are



observed for large amplitude dust devils passing close to SEIS. Acceleration signals are about  $0.5 \mu\text{ms}^{-2}$  on the horizontal and vertical components at 10 s period. Converting the horizontal acceleration values into tilt and rotation rate yields maximum rotation rates in the order of  $0.1 \mu\text{rads}^{-1}$ .

The maximum observed amplitude spectral density of a marsquake over 8 months of InSight operations was  $0.5 \mu\text{ms}^{-2}$  around 2.5 Hz, with several more events with amplitude levels larger than  $0.1 \mu\text{ms}^{-2}$  between 1 and 10 Hz. Assuming that the scattered coda contains mainly S-wave energy and that the S-wave velocity in the upper kilometer is around  $500 \text{ms}^{-1}$  for the poorly consolidated sediments that make up much of the Martian planes, we can estimate expected rotational rate levels in the order of  $0.2 \text{nrads}^{-1}\text{Hz}^{-1/2}$ .

For the HP<sup>3</sup> hammering as an example of an active-source seismic investigation, the maximum recorded acceleration amplitude was  $12 \text{mms}^{-2}$  for a bandpassed signal between 1 and 50 Hz with a resulting amplitude level of  $2 \text{mms}^{-2}\text{Hz}^{-1/2}$ . Assuming that waves at these high frequencies travel mainly in the shallowest layers, the relevant phase velocity is approximately  $100 \text{ms}^{-1}$ , resulting in a rotational amplitude level of  $20 \mu\text{rads}^{-1}\text{Hz}^{-1/2}$  for the signal peak. The minimum signal levels for active seismic investigations is expected to be similar to what was observed on the Moon during the Apollo 17 Active Seismic Experiment.

### Discussion and conclusions

6DoF sensors can significantly improve the science return of future space missions by opening new research opportunities. We presented signal levels in terms of translational acceleration and rotation rate as expected from

- Tracking a lander’s trajectory including rebounds and touchdown as well as local gravity measurements.
- Planetary objects or asteroids librations and tidal accelerations.
- Seismic ground motions.

In addition, we presented basic performance characteristics of state-of-the-art rotation and acceleration sensors commonly used in Earth sciences. Figures 5, 6, 7, 8 and 9 summarize expected signal levels for the set of target objects Dimorphos, Phobos, Europa, the Earth’s Moon, and Mars. The signal levels are compared to instrument self-noise levels of state-of-the-art sensors. For translational acceleration sensing, we include the very broad band (VBB) sensor and short-period (SP) sensor of SEIS on the InSight mission (Lognonné et al. 2019), the long-period (LP) instrument from the Apollo mission (Nunn et al. 2020), and the STS2 seismometer (Sleeman and Melichar 2012). For rotation rate sensing, we include the LCG-Demonstrator from Litef, Germany (Bernauer et al. 2012), the blueSeis-3A from iXblue, France, (Bernauer et al. 2018) and the giant fiber-optic gyroscope FARO (by Streckeisen). We also show ambient noise recordings

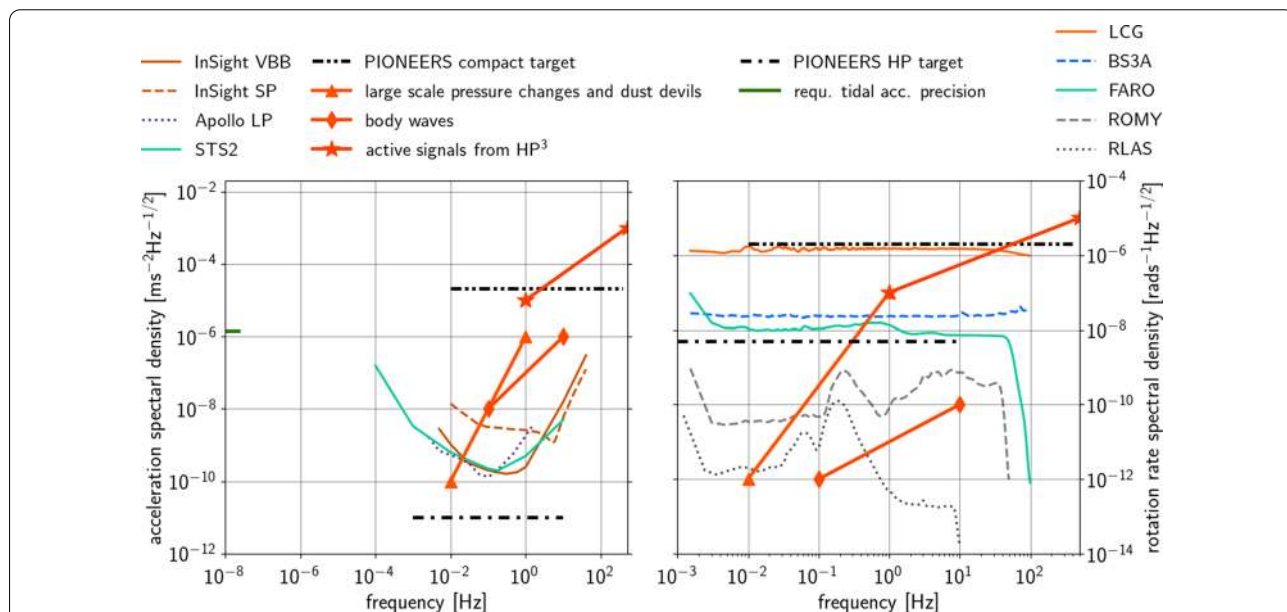


**Fig. 9** Expected signal levels on Mars. For forced librations and tidal accelerations, the required resolution is shown. Additionally, self-noise levels of commonly used sensors are shown (see Fig. 5)

from large ring-laser gyroscopes RLAS located in Wettzell, Germany, and ROMY located in Fürstfeldbruck, Germany.

Comparing the expected signal levels to the target self-noise levels of the instruments developed within the PIONEERS framework, leads to the following conclusions: The PIONEERS Compact model (the accelerometer as well as the rotational motion sensor) can resolve signals from lander–surface interactions during the free-fall landing process on asteroids and asteroid-like objects (Figs. 5, 6). The PIONEERS high-performance prototype is designed to be able to resolve large forced libration amplitudes as, for example expected from a binary system like Didymos. However, to be able to resolve forced librations at a level that allows constraining interior models of other planetary objects special emphasis must be placed on long term stability (Figs. 7, 8 and 9).

The PIONEERS compact model as well as the high-performance prototype make active 6DoF seismology possible on planetary objects or asteroids. The science case of 6DoF seismology requires active sources generating large amplitude signals. In its present state, the PIONEERS compact model is not able to resolve the passive seismic signals considered in this study.

The PIONEERS high-performance prototype instrument will be able to resolve most of the passive seismic translational acceleration signals considered in this study with frequencies below 10 Hz. The high-performance rotation rate sensor is expected to record seismic rotational ground motions originating from meteoroid impacts, artificial impacts and active seismic sources. On small bodies it can record tidal events and thermal cracks (Figs. 5 and 6). However, for 6DoF passive seismology on large objects, the self-noise level of the high-performance rotational motion sensor has to be improved by 1–2 orders of magnitude.

Even though the sensitivity of current rotation rate sensors might not be sufficient to fully exploit the advantages of precise 6DoF observations for planetary exploration, the compact model requirements allow to measure lander–surface interactions and active seismic signals on asteroids and planetary objects. Probing near-surface mechanical properties of asteroids and planetary objects with active seismic experiments involving 6DoF instruments requires a relatively short mission duration compared to the mission duration required for passive seismic experiments in seismically very quiet planetary environments. In addition, the compact model can serve as a high-grade inertial measurement unit for navigation of orbiter and lander and improves local gravity field determination. Therefore, we want to encourage future mission planners to

consider including high-precision 6DoF instruments to their mission design.

#### Acknowledgements

The presented investigation is part of the project PIONEERS (Planetary Instruments based on Optical technologies for an Innovative European Exploration using Rotational Seismology) funded by the Horizon 2020 research and innovation program of the European Commission.

#### Authors' contributions

FB wrote the manuscript and coordinated the work leading to the scientific requirements definitions. RFG is the PIONEERS project coordinator and contributed to the lander–surface interaction section and estimated rotational seismic noise from atmospheric processes on Mars. NM contributed to the lander–surface interaction section. VD, BR, VF, and OK contributed to the rotational dynamics and tidal acceleration section. DS, SC, and SS, contributed to the 6DoF section with a focus on seismic signals on the Moon and on Mars. JW, HI, JR, and DG contributed to the 6DoF seismology section. AC, DM, FG, GL, LF, JJB and SdR are the PIONEERS leading Instrument developers who contributed to the Instruments and Technologies section

#### Funding

Open Access funding enabled and organized by Projekt DEAL. The research for this study was part of the PIONEERS-project that has received funding from the European Union's Horizon 2020 research and innovation program under grant agreement number 821881. We also acknowledge support from the ERC-Advanced project ROMY (No. 339991).

#### Availability of data and materials

The data sets used and/or analyzed during the current study are available from the corresponding author on reasonable request.

#### Competing interests

The authors declare that they have no competing interests.

#### Author details

<sup>1</sup> Department für Geo- und Umweltwissenschaften, Ludwig-Maximilians Universität München (LMU), 80333 München, Germany. <sup>2</sup> ISAE-SUPAERO, 31055 Toulouse, France. <sup>3</sup> Royal Observatory of Belgium, 1180 Uccle, Belgium. <sup>4</sup> Department of Earth Sciences, ETH Zürich, 8092 Zürich, Switzerland. <sup>5</sup> iXblue, 78100 Saint-Germain-en-Laye, France. <sup>6</sup> Institute de Physique du Globe de Paris, 75205 Paris, France.

Received: 23 August 2020 Accepted: 6 December 2020

Published online: 21 December 2020

#### References

- Van den Acker E, Van Hoolst T, de Viron O, Defraigne P, Forget F, Hourdin F, Dehant V (2002) Influence of the seasonal winds and the CO<sub>2</sub> mass exchange between atmosphere and polar caps on Mars' rotation. *J Geophys Res* 107:1–8
- Banerdt WB, Smrekar SE, Banfield D, Giardini D, Golombek M, Johnson CL, Lognonné P, Spiga A, Spohn T, Perrin C, Stähler SC, Antonangeli D, Asmar S, Beghein C, Bowles N, Bozdog E, Chi P, Christensen U, Clinton J, Collins GS, Daubar I, Dehant V, Drilleau M, Fillingim M, Folkner W, Garcia RF, Garvin J, Grant J, Grott M, Grygorczuk J, Hudson T, Irving JCE, Kargl G, Kawamura T, Kedar S, King S, Knapmeyer-Endrun B, Knapmeyer M, Lemmon M, Lorenz R, Maki JN, Margerin L, McLennan SM, Michaut C, Mimoun D, Mittelholz A, Mocquet A, Morgan P, Mueller NT, Murdoch N, Nagihara S, Newman C, Nimmo F, Panning M, Pike WT, Plesa AC, Rodriguez S, Rodriguez-Manfredi JA, Russell CT, Schmerr N, Siegler M, Stanley S, Stutzmann E, Teanby N, Tromp J, van Driel M, Warner N, Weber R, Wieczorek M (2020) Initial results from the insight mission on Mars. *Nat Geosci* 13:183–189
- Barnouin O, Daly M, Palmer E, Johnson C, Gaskell R, Al Asad M, Bierhaus E, Craft K, Ernst C, Espiritu R, Nair H, Neumann G, Nguyen N, Nolan M, Mazarico E, Perry M, Philpott L, Roberts J, Steele R, Seabrook J, Susorney H, Weirich J, Lauretta D (2020) Digital terrain mapping by the osiris-REX mission. *Planet Space Sci* 180:104764. <https://doi.org/10.1016/j.pss.2019.104764>

- Berger J, Davis P, Widmer-Schniedrig R, Zumberge M (2014) Performance of an optical seismometer from 1  $\mu$ hz to 10 hz. *Bull Seismol Soc Am* 104:2422–2429
- Bernauer F, Wassermann J, Guattari F, Frenois A, Bigueur A, Gaillot A, de Toldi E, Ponceau D, Schreiber U, Igel H (2018) BlueSeis3A: full characterization of a 3C broadband rotational seismometer. *Seismol Res Lett* 89:620–629
- Bernauer F, Wassermann J, Igel H (2012) Rotational sensors: a comparison of different sensor types. *J Seismol* 16:595–602
- Bernauer F, Wassermann J, Igel H (2020) Dynamic tilt correction using direct rotational motion measurements. *Seismol Res Lett*. <https://doi.org/10.1785/0220200132>
- Bernauer M, Fichtner A, Igel H (2014) Reducing nonuniqueness in finite source inversion using rotational ground motions. *J Geophys Res* 119:4860–4875
- Biele J, Ulamec S, Maibaum M, Roll R, Witte L, Jurado E, Muñoz P, Arnold W, Auster HU, Casas C, Faber C, Fantinati C, Finke F, Fischer HH, Geurts K, Güttler C, Heinisch P, Herique A, Hviid S, Kargl G, Knapmeyer M, Knollenberg J, Kofman W, Kömle N, Kührt E, Lommatsch V, Mottola S, Pardo de Santayana R, Remetean E, Scholten F, Seidensticker KJ, Sierks H, Spohn T (2015) The landing(s) of philaee and inferences about comet surface mechanical properties. *Science*. <https://doi.org/10.1126/science.aaa9816>
- Bolstad P, Stowe T (1994) An evaluation of dem accuracy: elevation, slope, and aspect. *Photogramm Eng Remote Sens* 60:1327–1332
- Bormann P, Wielandt E (2013) Seismic Signals and Noise, in: Bormann, P. (Ed.), *New Manual of Seismological Observatory Practice 2 (NMSOP2)*. Deutsches GeoForschungsZentrum GFZ, Potsdam, pp. 1–62. [https://doi.org/10.2312/GFZ.NMSOP-2\\_ch4](https://doi.org/10.2312/GFZ.NMSOP-2_ch4)
- Carroll KA, Faber DR (2018) Asteroid Orbital Gravity Gradiometry. In: *Lunar and Planetary Science Conference*, p. 1231
- Cheng A, Michel P, Jutzi M, Rivkin A, Stickle A, Barnouin O, Ernst C, Atchison J, Pravec P, Richardson D (2016) Asteroid impact & deflection assessment mission: Kinetic impactor. *Planet Space Sci* 121:27–35
- Crawford WC, Webb SC (2000) Identifying and removing tilt noise from low-frequency (< 0.1 hz) seafloor vertical seismic data. *Bull Seismol Soc Am* 90:952–963
- Delbo M, Libourel G, Wilkerson J, Murdoch N, Michel P, Ramesh KT, Ganino C, Verati C, Marchi S (2014) Thermal fatigue as the origin of regolith on small asteroids. *Nature* 508:233–236
- Donner S, Bernauer M, Igel H (2016) Inversion for seismic moment tensors combining translational and rotational ground motions. *Geophys J Int* 207:562–570
- Donner S, Bernauer M, Reinwald M, Hadziioannou C, Igel H (2017) Improved source inversion from joint measurements of translational and rotational ground motions. *AGU Fall Meeting, Abstract S44B–04*
- Duennebr F, Sutton GH (1974) Thermal moonquakes. *J Geophys Res* 1896–1977(79):4351–4363
- ESA, (2019) Esa strategy for science at the moon. <http://exploration.esa.int/moon/61371-esa-strategy-for-science-at-the-moon/#>. Accessed June 2020
- Folkner WM, Dehant V, Le Maistre S, Yseboodt M, Rivoldini A, Van Hoolst T, Asmar SW, Golombek MP (2018) The rotation and interior structure experiment on the insight mission to mars. *Space Sci Rev*. <https://doi.org/10.1007/s11214-018-0530-5>
- Frohlich C, Nakamura Y (2009) The physical mechanisms of deep moonquakes and intermediate-depth earthquakes: How similar and how different? *Phys Earth Planet Inter* 173:365–374
- Garcia RF, Kenda B, Kawamura T, Spiga A, Murdoch N, Lognonné PH, Widmer-Schniedrig R, Compaigne N, Orhand-Mainsant G, Banfield D et al (2020) Pressure effects on the seis-insight instrument, improvement of seismic records, and characterization of long period atmospheric waves from ground displacements. *Journal of Geophysical Research: Planets*. <https://doi.org/10.1029/2019JE006278>
- Garcia RF, Khan A, Drilleau M, Margerin L, Kawamura T, Sun D, Wiczeorek MA, Rivoldini A, Nunn C, Weber RC et al (2019) Lunar seismology: An update on interior structure models. *Space Science Reviews*. <https://doi.org/10.1007/s11214-019-0613-y>
- Giardini D, Lognonné P, Banerdt WB, Pike WT, Christensen U, Ceylan S, Clinton JF, van Driel M, Stähler SC, Böse M, Garcia RF, Khan A, Panning M, Perrin C, Banfield D, Beucler E, Charalambous C, Euchner F, Horleston A, Jacob A, Kawamura T, Kedar S, Mainsant G, Scholz JR, Smrekar SE, Spiga A, Agard C, Antonangeli D, Barkaoui S, Barrett E, Combes P, Conejero V, Daubar I, Drilleau M, Ferrier C, Gabsi T, Gudkova T, Hurst K, Karakostas F, King S, Knapmeyer M, Knapmeyer-Endrun B, Llorca-Cejudo R, Lucas A, Luno L, Margerin L, McClean JB, Mimoun D, Murdoch N, Nimmo F, Nonon M, Pardo C, Rivoldini A, Manfredi JAR, Samuel H, Schimmel M, Stott AE, Stutzmann E, Teanby N, Warren T, Weber RC, Wiczeorek M, Yana C (2020) The seismicity of mars. *Nat Geosci* 13:205–212
- Goldman DI, Umbanhowar P (2008) Scaling and dynamics of sphere and disk impact into granular media. *Phys Rev E*. <https://doi.org/10.1103/PhysRevE.77.021308>
- Hadziioannou C, Gaebler P, Schreiber U, Wassermann J, Igel H (2012) Examining ambient noise using colocated measurements of rotational and translational motion. *J Seismol* 16:787–796
- Ho TM, Baturkin V, Grimm C, Grundmann JT, Hobbie C, Ksenik E, Lange C, Sasaki K, Schlotterer M, Talapina M, Termtanasombat N, Wejmo E, Witte L, Wrasmann M, Wübbels G, Rößler J, Ziach C, Findlay R, Biele J, Krause C, Ulamec S, Lange M, Mierheim O, Lichtenheldt R, Maier M, Reill J, Sedlmayr HJ, Bousquet P, Bellion A, Bompis O, Cenac-Morthe C, Deleuze M, Fredon S, Jurado E, Canalias E, Jaumann R, Bibring JP, Glassmeier KH, Hercic D, Grott M, Celotti L, Cordero F, Hendrikse J, Okada T (2017) Mascot—the mobile asteroid surface scout onboard the hayabusa2 mission. *Space Sci Rev* 208:339–374
- Huang Q, Wiczeorek MA (2012) Density and porosity of the lunar crust from gravity and topography. *J Geophys Res*. <https://doi.org/10.1029/2012JG004062>
- Hurford TA, Asphaug E, Spitale JN, Hemingway D, Rhoden AR, Henning WG, Bills BG, Kattenhorn SA, Walker M (2016) Tidal disruption of phobos as the cause of surface fractures. *J Geophys Res* 121:1054–1065
- Igel H, Bernauer M, Wassermann J, Schreiber KU (2015) Seismology, rotational, complexity. In: Meyers RA (ed) *Encyclopedia of complexity and systems science*. Springer, New York, pp 1–26
- Kaspi Y, Hubbard WB, Showman AP, Flierl GR (2010) Gravitational signature of Jupiter's internal dynamics. *Geophys Res Lett*. <https://doi.org/10.1029/2009GL041385>
- Keil S, Wassermann J, Igel H (2020) Single-station seismic microzonation using 6c measurements. *J Seismol*. <https://doi.org/10.1007/s10950-020-09944-1>
- Khan A, van Driel M, Böse M, Giardini D, Ceylan S, Yan J, Clinton J, Euchner F, Lognonné P, Murdoch N, Mimoun D, Panning M, Knapmeyer M, Banerdt WB (2016) Single-station and single-event Marsquake location and inversion for structure using synthetic Martian waveforms. *Phys Earth Planet Inter* 258:28–42
- Konopliv AS, Park RS, Folkner WM (2016) An improved JPL Mars gravity field and orientation from Mars orbiter and lander tracking data. *Icarus* 274:253–260
- Krijt J, Güttler C, Heißelmann D, Dominik C, Tielens AGGM (2013) Energy dissipation in head-on collisions of spheres. *J Phys D*. <https://doi.org/10.1088/0022-3727/46/43/435303>
- Kunze AWG (1974) Lunar crustal density profile from an analysis of Doppler gravity data. In: *Lunar and planetary science conference*, p. 428
- Kuramoto K, Kawakatsu Y, Fujimoto M, MMX Study Team (2017) Martian moons exploration (MMX) conceptual study results. In: *Lunar and planetary science conference*, p. 2086
- Lammlein DR (1977) Lunar seismicity and tectonics. *Phys Earth Planet Inter* 14:224–273
- Lammlein DR, Latham GV, Dorman J, Nakamura Y, Ewing M (1974) Lunar seismicity, structure, and tectonics. *Rev Geophy* 12:1–21
- Latham G, Ewing M, Dorman J, Lammlein D, Press F, Toksoz N, Sutton G, Duennebr F, Nakamura Y (1971) Moonquakes. *Science* 174:687–692
- Latham G, Ewing M, Press F, Sutton G (1969) The apollo passive seismic experiment. *Science* 165:241–250
- Mv Laue (1911) Über einen Versuch zur Optik der bewegten Körper. *Münchener Sitzungsberichte* 12:405–412
- Le Maistre S, Rivoldini A, Rosenblatt P (2019) Signature of phobos' interior structure in its gravity field and libration. *Icarus* 321:272–290
- Lee S, Zanolin M, Thode AM, Pappalardo RT, Makris NC (2003) Probing europa's interior with natural sound sources. *Icarus* 165:144–167
- Lefèvre HC (2014) *The fiber-optic gyroscope*, 2nd edn. Artech House, London
- Lognonné P, Banerdt WB, Pike WT, Giardini D, Christensen U, Garcia RF, Kawamura T, Kedar S, Knapmeyer-Endrun B, Margerin L, Nimmo F, Panning M, Tauzin B, Scholz JR, Antonangeli D, Barkaoui S, Beucler E, Bissig F, Brinkman N, Calvet M, Ceylan S, Charalambous C, Davis P, van Driel M, Drilleau M, Fayon L, Joshi R, Kenda B, Khan A, Knapmeyer M, Lekic



- V, McClean J, Mimoun D, Murdoch N, Pan L, Perrin C, Pinot B, Pou L, Menina S, Rodriguez S, Schmelzbach C, Schmitt N, Sollberger D, Spiga A, Stähler S, Stott A, Stutzmann E, Tharimena S, Widmer-Schmid R, Andersson F, Ansan V, Beghein C, Böse M, Bozdogan E, Clinton J, Daubar I, Delage P, Fuji N, Golombek M, Grott M, Horleston A, Hurst K, Irving J, Jacob A, Knollenberg J, Krasner S, Krause C, Lorenz R, Michaut C, Myhill R, Nissen-Meyer T, ten Pierick J, Plesa AC, Quantin-Nataf C, Robertsson J, Rochas L, Schimmel M, Smrekar S, Spohn T, Teanby N, Tromp J, Vallade J, Verdier N, Vrettos C, Weber R, Banfield D, Barrett E, Bierwirth M, Calcutt S, Compaire N, Johnson CL, Mance D, Euchner F, Kerjean L, Mainsant G, Mocquet A, Rodriguez Manfredi JA, Pont G, Laudet P, Nebut T, de Raucourt S, Robert O, Russell CT, Sylvestre-Baron A, Tillier S, Warren T, Wieczorek M, Yana C, Zweifel P (2020) Constraints on the shallow elastic and anelastic structure of mars from insight seismic data. *Nat Geosci* 13:213–220
- Lognonné P, Banerdt WB, Giardini D, Pike WT, Christensen U, Laudet P, de Raucourt S, Zweifel P, Calcutt S, Bierwirth M et al (2019) Seis: Insight's seismic experiment for internal structure of mars. *Space Sci Rev*. <https://doi.org/10.1007/s11214-018-0574-6>
- McGovern PJ, Solomon SC, Smith DE, Zuber MT, Simons M, Wieczorek MA, Phillips RJ, Neumann GA, Aharonson O, Head JW (2002) Localized gravity/topography admittance and correlation spectra on mars: Implications for regional and global evolution. *J Geophys Res* 107:1–25
- Michel P, Küppers M, Carnelli I (2018) The Hera mission: European component of the ESA-NASA AIDA mission to a binary asteroid, in: 42nd COSPAR Scientific Assembly, pp. B1.1–42–18
- Minshull T, Gouly N (1988) The influence of tidal stresses on deep moonquake activity. *Phys Earth Planet Inter* 52:41–55
- Murdoch N, Avila Martinez I, Sunday C, Zenou E, Cherrier O, Cadu A, Gourinat Y (2017) An experimental study of low-velocity impacts into granular material in reduced gravity. *Monthly Notices R Astronom Soc* 1:1. <https://doi.org/10.1093/mnras/stw3391>
- Murdoch N, Hempel S, Pou L, Cadu A, Garcia RF, Mimoun D, Margerin L, Karatekin O (2017) Probing the internal structure of the asteroid Didymos with a passive seismic investigation. *Planet Space Sci* 144:89–105
- Murdoch N, Sánchez P, Schwartz SR, Miyamoto H (2015) Asteroid surface geophysics. In: Michel P, DeMeo FE, Bottke WF (eds) *Asteroids IV*. University of Arizona Press, Tucson, pp 767–792
- Naidu SP, Margot JL (2015) Near-Earth Asteroid Satellite Spins Under Spin-Orbit Coupling. *The Astronomical Journal*. <https://doi.org/10.1088/0004-6256/149/2/80>
- Nakamura Y (2003) New identification of deep moonquakes in the apollo lunar seismic data. *Phys Earth Planet Inter* 139:197–205
- Nakamura Y (2005) Farside deep moonquakes and deep interior of the moon. *J Geophys Res*. <https://doi.org/10.1029/2004JE002332>
- Nakamura Y, Latham GV, Dorman HJ (1982) Apollo lunar seismic experiment—final summary. *J Geophys Res* 87:A117–A123
- Nunn C, Garcia RF, Nakamura Y, Marusiak AG, Kawamura T, Sun D, Margerin L, Weber R, Drilleau M, Wieczorek MA, Khan A, Rivoldini A, Lognonné P, Zhu P (2020) Lunar seismology: a data and instrumentation review. *Space Sci Rev* 2:6. <https://doi.org/10.1007/s11214-020-00709-3>
- Oberst J, Nakamura Y (1991) A search for clustering among the meteoroid impacts detected by the apollo lunar seismic network. *Icarus* 91:315–325
- Panning M, Lecik V, Manga M, Cammarano F, Romanowicz B (2006) Long-period seismology on europa: 2. Predicted seismic response. *J Geophys Res*. <https://doi.org/10.1029/2006JE002712>
- Panning MP, Beucler Éric, Drilleau M, Mocquet A, Lognonné P, Banerdt WB (2015) Verifying single-station seismic approaches using earth-based data: Preparation for data return from the insight mission to mars. *Icarus* 248:230–242
- Panning MP, Stähler SC, Huang HH, Vance SD, Kedar S, Tsai VC, Pike WT, Lorenz RD (2018) Expected seismicity and the seismic noise environment of europa. *J Geophys Res* 123:163–179
- Pappalardo R, Vance S, Bagenal F, Bills B, Blaney D, Blankenship D, Brinckerhoff W, Connerney J, Hand K, Hoehler T, Leisner J, Kurth W, McGrath M, Mellon M, Moore J, Patterson G, Prockter L, Senske D, Schmidt B, Shock E, Smith D, Soderlund K (2013) Science potential from a europa lander. *Astrobiology* 13:740–773
- Rambaux N, Williams JG (2011) The Moon's physical librations and determination of their free modes. *Celest Mech Dyn Astron* 109:85–100
- Reinwald M, Bernauer M, Igel H, Donner S (2016) Improved finite-source inversion through joint measurements of rotational and translational ground motions: a numerical study. *Solid Earth* 7:1467–1477
- Richardson DC, Barnouin OS, Benner LAM, Bottke W, Campo Bagatin A, Cheng AF, Eggl S, Hamilton DP, Hestroffer D, Hirabayashi M, Maurel C, McMahon JW, Michel P, Murdoch N, Naidu SP, Pravec P, Rivkin AS, Rosenblatt P, Sarid G, Scheeres DJ, Scheirich P, Tsiganis K, Zhang Y, AIDA Dynamical and Physical Properties of Didymos Working Group (2016) Dynamical and Physical Properties of 65803 Didymos, the Proposed AIDA Mission Target, in: AAS/Division for Planetary Sciences Meeting Abstracts #48, p. 123.17
- Sagnac G (1913) L'éther lumineux démontré par l'effet du vent relatif déther dans un interféromètre en rotation uniforme. *Comptes Rendus* 157:708–710
- Schmelzbach C, Donner S, Igel H, Sollberger D, Taufiqurrahman T, Bernauer F, Häusler M, van Renterghem C, Wassermann J, Robertsson J (2018) Advances in 6c seismology: applications of combined translational and rotational measurements in global and exploration seismology. *Geophysics* 83:WC53–WC69
- Sens-Schönfelder C, Larose E (2010) Lunar noise correlation, imaging and monitoring. *Earthq Sci* 23:519–530
- Sleeman R, Melichar P (2012) A PDF representation of the STS-2 self-noise obtained from one year of data recorded in the conrad observatory, Austria. *Bull Seismol Soc Am* 102:587–597
- Sollberger D, Greenhalgh SA, Schmelzbach C, Van Renterghem C, Robertsson JOA (2018) 6-c polarization analysis using point measurements of translational and rotational ground-motion: theory and applications. *Geophys J Int* 213:77–97
- Sollberger D, Schmelzbach C, Robertsson JOA, Greenhalgh SA, Nakamura Y, Khan A (2016) The shallow elastic structure of the lunar crust: new insights from seismic wavefield gradient analysis. *Geophys Res Lett* 43:10078–10087
- Sorrells GG (1971) A preliminary investigation into the relationship between long-period seismic noise and local fluctuations in the atmospheric pressure field. *Geophys J Int* 26:71–82
- Spudich P, Steck LK, Hellweg M, Fletcher JB, Baker LM (1995) Transient stresses at parkfield, california, produced by the m 7.4 landers earthquake of june 28, 1992: Observations from the upsar dense seismograph array. *J Geophys Res* 100:675–690
- Streckeisen G (1995) Portable Very-Broad-Band Tri-Axial Seismometer: STS-2 Low Power. G. Streckeisen AG. CH-8244 Pfungen, Switzerland
- Stähler SC, Panning MP, Vance SD, Lorenz RD, van Driel M, Nissen-Meyer T, Kedar S (2018) Seismic wave propagation in icy ocean worlds. *J Geophys Res* 123:206–232
- Talwani M, Kahle HG (1976) Apollo 17 traverse gravimeter experiment/preliminary results/. NASA STI/Recon Tech Rep A 77:85–91
- Tanimoto T, Hadziioannou C, Igel H, Wassermann J, Schreiber U, Gebauer A (2015) Estimate of Rayleigh-to-Love wave ratio in the secondary microseism by co-located ring laser and seismograph. *Geophys Res Lett* 1:1. <https://doi.org/10.1002/2015GL063637>
- Tanimoto T, Valocin A (2016) Existence of the threshold pressure for seismic excitation by atmospheric disturbances. *Geophys Res Lett* 43:11202–11208
- Ulamet S, Fantinati C, Maibaum M, Geurts K, Biele J, Jansen S, Küchemann O, Cozzoni B, Finke F, Lommatsch V, Moussi-Soffys A, Delmas C, O'Rourke L (2016) Rosetta lander - landing and operations on comet 67p/churyumov-gerasimenko. *Acta Astronautica* 125:80–91
- Van Hoolst T, Baland RM, Trinh A (2013) On the librations and tides of large icy satellites. *Icarus* 226:299–315
- Vance SD, Kedar S, Panning MP, Stähler SC, Bills BG, Lorenz RD, Huang HH, Pike W, Castillo JC, Lognonné P, Tsai VC, Rhoden AR (2018) Vital signs: Seismology of icy ocean worlds. *Astrobiology* 18:37–53
- Wassermann J, Bernauer F, Shiro B, Johanson I, Guattari F, Igel H (2020) Six-axis ground motion measurements of caldera collapse at kilauea volcano, hawaii - more data, more puzzles? *Geophysical Research Letters*. <https://doi.org/10.1029/2019GL085999>
- Wassermann J, Wietek A, Hadziioannou C, Igel H (2016) Toward a single-station approach for microzonation: using vertical rotation rate to estimate love-wave dispersion curves and direction finding. *Bull Seismol Soc Am* 106:1316–1330

Wielandt E (2012) Seismic Sensors and their Calibration, in: Bormann, P. (Ed.), *New Manual of Seismological Observatory Practice 2 (NMSOP-2)*. Deutsches GeoForschungsZentrum GFZ, Potsdam. volume 2, pp. 1 – 51

Willner K, Oberst J, Hussmann H, Giese B, Hoffmann H, Matz KD, Roatsch T, Duxbury T (2010) Phobos control point network, rotation, and shape. *Earth Planet Sci Lett* 294:541–546

Yuan S, Simonelli A, Lin C, Bernauer F, Donner S, Braun T, Wassermann J, Igel H (2020) Six degree-of-freedom broadband ground-motion observations with portable sensors: validation, local earthquakes, and signal processing. *Bull Seismol Soc Am* 110:953–969

### **Publisher's Note**

Springer Nature remains neutral with regard to jurisdictional claims in published maps and institutional affiliations.